Full Paper

A Whole Explosive Dispersion Process Prediction Model for Fuel Clouds

Xing Chen,[a, b] Zhongqi Wang,*[a] and Yun Liu[c]

Abstract: The study of the liquids and granular materials dispersed by high explosions is of great significance in the fuel-air-explosion and petrochemical fields. However, there is minimal dynamic dispersal research at high speed. Therefore, the numerical calculation methods of explosive dispersion have become a priority. A model is proposed that can predict the characteristics of the explosive dispersal for fuel both in the near-field and the far-field. Then, the basic laws of the fuel cloud formed during explosive dispersal are derived. The model is constructed by six parts of different processes, with the characteristics obtained by tracking the fuel droplets or particles and calculating their velocity, displacement, mass, and particle size. This model is validated using two sets of experimental data consisting of dynamic fuel dispersion and static fuel dispersion that fit the model well.

Keywords: Explosive dispersion · Dynamic fuel dispersion · Predictive model · Heterogeneous explosive · Particle jets

1 Introduction

If a cylinder explosive charge is surrounded by solid particles or a layer of liquid, when the charge is detonated, it drives the liquid or solid particles through the high-pressure and high-temperature explosive products, which are dispersed and form a fuel cloud. Therefore, explosive dispersal has tremendous power, as witnessed in leakage accidents of hydrocarbon fuels involved in petroleum, natural gas, plastics, and rubber industries as raw materials. In particular, petroleum has frequently experienced detonation in the surrounding area and has formed multiple points of explosive dispersion, causing a wide disaster range. From another perspective, in the military, a series of weapons, such as the fuel-air-explosion, cannon guns, and automatic grenade launchers, have been developed by exploiting the characteristics of the fuel-air mixture, and this mixture can be used as fuel in aviation bombs, individual grenades, rockets, or missile warheads. Therefore, it is valuable to research the explosive dispersal process of a fuel cloud.

There are few studies on dynamic cloud dispersal, especially at high speeds. Because of the high cost and difficulty of dynamic cloud testing, trying to solve these problems through testing is very difficult. Therefore, studying the predictive model of dynamic dispersal to improve the safety and reliability of cloud detonation is urgently required. For static fuel dispersal, the current models only describe a part of the explosive dispersal process or lack the initial conditions when connecting the near-field and far-field. Therefore, it is of great importance to present a model that can predict the whole process of explosive dispersal in both the near-field and far-field and predict the initial conditions such as the cloud radius, cloud velocity, and particle size. Establishing a model to study the formation of cloud deto-

nation is of great consequence for further study and prevention of the damaging effects caused by gas-cloud explosions. Such a model could also be used in the research of granular material and liquid dispersed by an explosive charge to simulate the characteristics before tests, making the results manageable. In this way, the actual experimental process saves more energy and is more efficient, safe, and effective.

Therefore, it is important to study the model of cloud detonation to lay the foundation for the development of extinguishing technology and provide technical services for the research and development of advanced weaponry and equipment.

According to aerodynamic forces and the inertia acting on the fuel, the cloud formation process is divided into three phases [1, 2]. During the first phase, the inertia force is the dominate force; in the second phase, the aerodynamic drag is comparable to inertia forces on the fuel; and during the third phase, the aerodynamic drag is larger than the inertia force and plays a leading role.

[a] *X. Chen, Z. Wang*
State Key Laboratory of Explosion Science and Technology
Beijing Institute of Technology
Beijing, 100081, China
*e-mail: 3120150152@bit.edu.cn
[b] *X. Chen*
College of Environment and Chemical Engineering
Sichuan University of Science & Engineering
Zigong, 643002, China
[c] *Y. Liu*
Commercial vehicle technology center
SAIC Motor Corp Ltd.
Shanghai, 200041, China

Frost et al. extended the Gurney method to the conical system to illustrate the dependence of velocity and coherency of the jet on the particle properties and the ratio of particle mass to explosive mass [3]. The results showed that the Gurney velocity for the conical system was less than the velocity of the spherical charge, which can be minimized by surrounding the cone with a heavy tamper. Ripley and Zhang analyzed the instability mechanism of jet formation, growth, and extinction during fuel dispersal and made a numerical analysis that showed the major jetting structure was defined by the internal interface instability; the number of jets was also defined by the instability induced by the fragments from the inner boundary [4]. Alonso et al. described the explosion process of a vapor cloud using the TNO (The Netherlands Organization) multi-energy model [5]. The curve provided by the model can obtain the function relation between the peak overpressure, specific impulse, and distance after data fitting. These studies provide a rich foundation for the theoretical study of explosive dispersal. Some important links and problems of explosive dispersal were also described by these models. However, there is a lack of models that comprehensively describe the whole process of explosive dispersal and the relationship between morphological characteristics of fuel cloud and the various parameters.

Frost et al. performed dispersal experiments for cylindrical geometry and concluded that a solid granular bed saturated with liquid generated more jets than either material alone during dispersal; the dispersal of a wet particle bed resulted in almost an order of magnitude more jets [6]. These jet formation effects have yet to be predicted by the current generation of multiphase models. Xue et al. used high-speed video to research the explosively driven dynamics of dry and wet sand and considered the jet formation by competition of inertial forces and viscous forces [7]. The results showed that multi-shear localizations rather than interface instability comprised the dominant mechanism for the onset of expanding sand. Milne et al. augmented high-speed video with X-ray data to improve upon this estimate and demonstrated that the fragmentation process started during the release wave from the outer radius, showing the characteristics of a brittle fracture mechanism in the condition of the surrounding loose powders [8]. Goroshin et al. developed the measurement for the changing of particle density with time during explosive dispersal based on laser light attenuation and there is good qualitative and quantitative correlation within 3 ms after detonation [9].

Loiseau et al. concluded that the terminal velocity of granular materials during explosive dispersal was over-predicted by the Gurney model because of the energy dissipated during the collapse of voids in the granular material bed [10]. They presented the empirical corrections that indirectly demonstrated that jetting during dispersal was caused by the failure of the shell and not the growth of interfacial instabilities. These studies provide abundant and powerful evidence for the jet formation mechanism, frag-

mentation time, and velocity of the high-energy explosives during explosive dispersal. Hezi Grisaro and Dancygier used the SPH (Smoothed Particle Hydrodynamics) method to simulate the fragment velocity distribution of charge and showed that the velocity distribution along cylinder axis was nonuniform, and the fragment velocity distribution can be described well by axisymmetric and 2D model techniques, which were relatively simple and required less computational resources [11]. Wang et al. measured the critical initiation energy of various mist/air mixtures by the up and down method, and obtained compared with the liquid-air mixtures, the critical initiation energy of gas-liquid-solid mixtures decreased while the detonation pressure and velocity significantly increased; the critical initiation energy was found to have a U-shaped curve relationship to the fuel-air ratio [12]. Zhang et al. divided the explosive dispersion process into the acceleration, deceleration, and turbulence phases of fuel dispersion [13]. A similarity law of fuel dispersing process was established using the dimensional analysis method and the effects of different length-diameter ratios and detonation locations on fuel particle velocity were simulated, providing theoretical guidance for the design of FAE (Fuel Air Explosion) weapons. Wang et al. used the commercial program (AUTODYN) and Gurney model to prove that the smaller ratio of center charge mass to fuel mass reduced the energy exchange between explosive products and air made more explosion energy convert into kinetic energy of particles [14]. According to the research of Bai et al. [15], the peak overpressure variation corresponding to different directions is directly related to the cloud cross-section. The propagation of the shock wave was affected by the forms of dispersal cloud to a large extent. These studies provide a theoretical basis for studying explosive dispersal and improving the security and effectiveness of explosive dispersal in applications.

All the presented studies have conducted modeling of various stages of explosive dispersal. However, few predictive models describe the whole process of explosive dispersal and provide the relationship between the development of a fuel cloud and the various parameters. The formation of a fuel cloud involves many complicated physical phenomena, such as the expansion of the liquid under the action of shock waves, crushing, and evaporation, causing the modeling to be difficult and complex.

In the present study, a model that can predict the variation of cloud movement during explosive dispersal process is proposed based on the combination and simplification of the near-field and far-field processes. This model can be used to describe the characteristics of a fuel cloud including the radius of the cloud, the speed of the cloud, and the size of drops or particles can be calculated in a few minutes. The model was validated by experimental data adopted from experiments and studies.

2 Modeling and Analyzing the Whole Process of Fuel Dispersal

To master the basic law of cloud formation during explosive dispersal, a theoretical model is needed to describe the process. The basic process of dispersal includes two phases. During the first phase, the fuel movement is dominated by the explosive force, whereas during the second phase, the fuel movement is dominated by aerodynamic drag.

The main characteristics of the former stage are the high-temperature and high-pressure detonation products formed by the central charge. Under the action of the detonation products, the shell is broken and the fuel ring expands and breaks to form large particles and droplets. During the latter stage, particles and droplets move in the air, forming gas-liquid or gas-solid-liquid multiphase clouds. The particles and droplets move through secondary crushing processes such as evaporation and stripping under the interaction between air and particles or droplets.

The basic dispersal structure is cylindrical. Therefore, the dispersal results and dispersal process of a single-center tube-type cylindrical dispersal structure are modeled, as shown in Figure 1. The cross-section of the cylindrical dispersal structure is shown in Figure 2.

In the study of cloud formation during explosive dispersion, cloud formation is affected by the explosive pressure of central charge and ambient air pressure and resistance force during explosive dispersal. The problems such as the detonation process of the central charge, cracking of the outer shell, initial crushing process of fuel liquids or granular materials, secondary crushing process of particles or droplets during flight need to be considered. These processes need to be modeled separately.

2.1 The Rigid Plastic Model of Shell Fracture under the Action of an Explosion

The shell breaking process is further simplified and the hypothesis condition is introduced: In the one-dimensional radial motion of the shell, the stress wave has been reflected many times in the deformation process of the shell. Consequently, the propagation of a stress wave is not discussed here. The elastic stage is not considered because of the large deformation of the shell and the rigid plastic material model is adopted. The shell stress state is shown in Figure 3.

In the one-dimensional radial motion of the shell, the stress wave has been reflected many times in the deformation process of the shell. Consequently, the propagation of a stress wave is not discussed here. The elastic stage is not considered because of the large deformation of the shell and the rigid plastic material model is adopted.

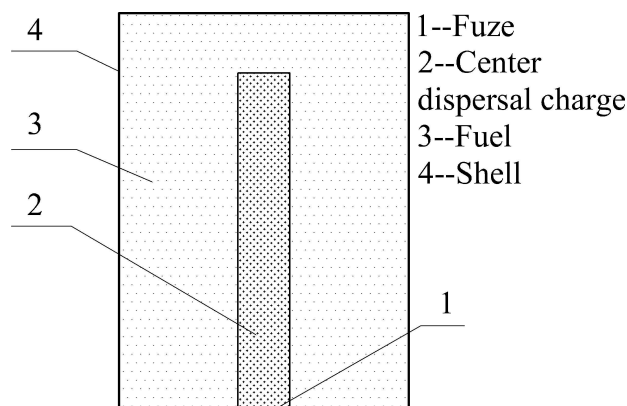This model can be obtained using the conservation of mass equations:

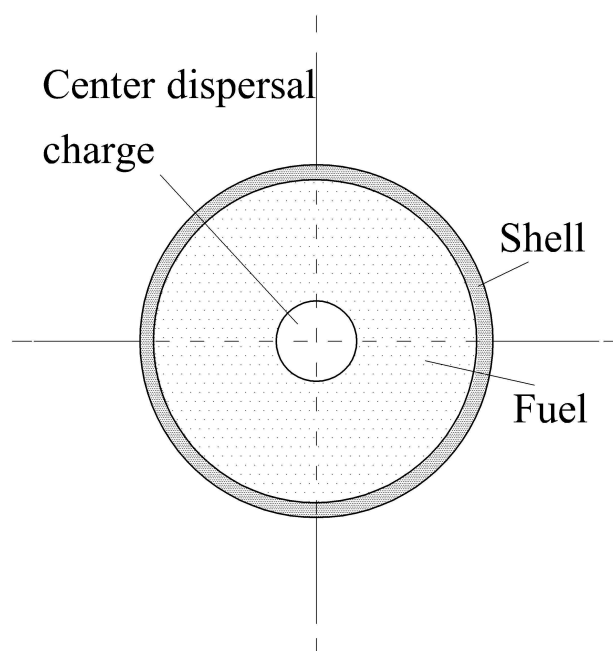**Figure 1.** The single-center tubular explosion dispersal structure.

Figure 2. The cross-section of the explosive dispersal structure.

$$r \frac{\partial \rho}{\partial t} = - \frac{\partial \rho u r}{\partial r} \tag{1}$$

$$\frac{\partial \rho}{\partial t} + \frac{\partial \rho u r}{\partial r} + \frac{\rho u}{r} = 0 \tag{2}$$

Eq. (1) and Eq. (2) are the continuity equations of mass conservation.

The symmetry of the problem indicates that no angular strain occurs at the four corners of the unit and the shear stress is zero. If the volume force is neglected, only the surface force σ_r and the surface forces σ_θ and σ_z can be applied. Because only the direction of r has mass transfer, momentum inflow and outflow only have r dependence. Thus,
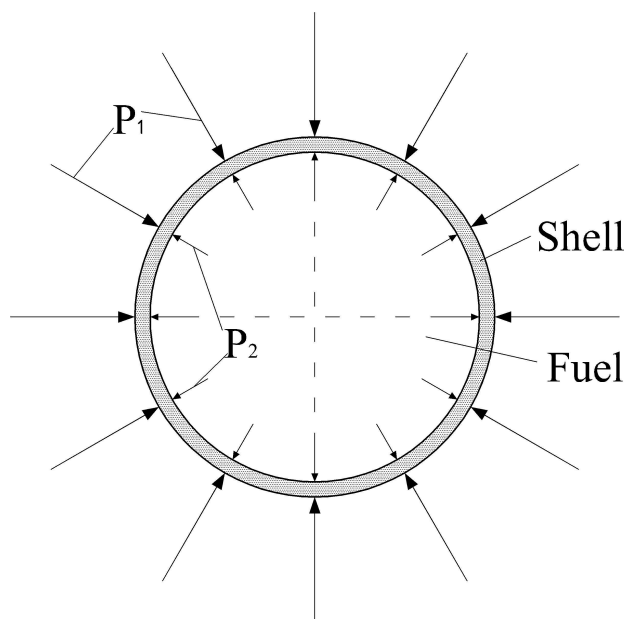
Figure 3. The shell stress state. (The shell expands under the internal pressure. P_2 is the pressure transmitted by the fuel on the inner surface of the shell; P_1 is the ambient air pressure on the outer surface.)

Eq. (3) can be obtained according to the momentum conservation condition:

$$\rho\left(\frac{\partial u}{\partial t} + u\frac{\partial u}{\partial t}\right) = \frac{\partial \sigma_r}{\partial r} + \frac{\sigma_r - \sigma_\theta}{\partial r} \tag{3}$$

Transferring to the Laplace coordinates results in the following equation:

$$\rho\frac{du}{dt} = \frac{\partial \sigma_r}{\partial r} + \frac{\sigma_r - \sigma_\theta}{\partial r} \tag{4}$$

This is the equation of motion in the direction of r obtained by the principle of momentum conservation. The failure of shell material is investigated by the Mises yield criterion. The expression of the misses yield criterion is:

$$(\sigma_1 - \sigma_2)^2 + (\sigma_2 - \sigma_3)^2 + (\sigma_3 - \sigma_1)^2 = 2\sigma_Y^D \tag{5}$$

In Eq. (5), σ_1, σ_2, and σ_3 are the main stress; while σ_Y^D is the dynamic yield stress for the material.

In the axisymmetric problem of a cylindrical coordinate system, σ_r, σ_θ, and σ_z are three principal stresses, which can be obtained based on plane strain conditions:

$$\sigma_z = \frac{1}{2}(\sigma_r + \sigma_\theta) \tag{6}$$

The Mises yield criterion can be written as:

$$(\sigma_\theta - \sigma_r)^2 = 1.15\sigma_Y^D \tag{7}$$

This equation can be used to solve the fracture radius of the shell and the initial velocity of the fragment by the continuous Eq. (1), the motion Eq. (3), Eq. (7), and boundary conditions.

Then, b and c represent the inner radius and outer radius of the shell in the deformation process respectively. u_b and u_c represent the particle velocities of the inner wall and outer wall of the shell.

The condition of ρ as a constant is substituted into Eq. (1):

$$\frac{\partial(ru)}{\partial r} = 0 \tag{8}$$

Therefore, u is not changing with r and it can be obtained at any radius r:

$$ru = bu_b \tag{9}$$

Differentiate Eq. (9) with time, and use $u = \frac{dr}{dt}$ and $u_b = \frac{db}{dt}$, yielding the following:

$$u^2 + r\frac{du}{dt} = u_b^2 + b\frac{du_b}{dt} \tag{10}$$

Thus, the following can be obtained:

$$\frac{du}{dt} = \frac{1}{r}\left(u_b^2 + b\frac{du_b}{dt}\right) - \frac{1}{r^3}b^2u_b^2 \tag{11}$$

By substituting Eq. (11) and (8) into Eq. (4), the equation of motion is transformed into Eq. (12):

$$\frac{\partial \sigma_r}{\partial r} + \frac{1.15\sigma_Y^D}{r} + \frac{\rho}{r}\left(u_b^2 + b\frac{du_b}{dt}\right) - \frac{b^2u_b^2\rho}{r^3} \tag{12}$$

Then, integrate r and obtain the following formula:

$$\sigma_r = 1.15\sigma_Y^D lnr + \rho\left[\left(u_b^2 + b\frac{du_b}{dt}\right)lnr + b\frac{u_b^2}{2r^2}\right] + C_1 \tag{13}$$

When the boundary condition is r=b and $\sigma_r = -P_2$, C_1 is defined as the following:

$$C_1 = -P_2 - 1.15\sigma_Y^D lnb - \rho\left[\left(u_b^2 + b\frac{du_b}{dt}\right)lnb - \frac{u_b^2}{2}\right] \tag{14}$$

$$\sigma_r = -P_2 + 1.15\sigma_Y^D ln\frac{r}{b} +$$
$$\rho\left[\left(u_b^2 + b\frac{du_b}{dt}\right)ln\frac{r}{b} - \frac{u_b^2}{2}\left(1 - \frac{b^2}{r^2}\right)\right] \tag{15}$$

The other two principal stresses can be obtained by substituting Eq. (7) and the plane strain condition:

$$-P_2 + 1.15\sigma_Y^D\left(1 + ln\frac{r}{b}\right) +$$
$$\rho\left[\left(u_b^2 + b\frac{du_b}{dt}\right)ln\frac{r}{b} - \frac{u_b^2}{2}\left(1 - \frac{b^2}{r^2}\right)\right] \tag{16}$$

$$\sigma_z = -P_2 + 1.15\sigma_Y^D\left(\frac{1}{2} + ln\frac{r}{b}\right) +$$
$$\rho\left[\left(u_b^2 + b\frac{du_b}{dt}\right)ln\frac{r}{b} - \frac{u_b^2}{2}\left(1 - \frac{b^2}{r^2}\right)\right] \tag{17}$$

Eq. (15), (16), and (17) are the stress distributions inside the shell with different radii. Under normal circumstances, the pressure at the inner wall of the shell P_2 is much greater than that of the yield stress σ_Y^D. Unless P_2 is reduced to σ_Y^D or even lower, σ_r and σ_θ of inner walls are both in the state of compressive stress.

$$\sigma_{r|a} = -P_2, \sigma_{\theta|a} = -P_2 + 1.15\sigma_Y^D \tag{18}$$

As r increases, the compressive stress value is decreased, yielding Eq. (16). In the case of $r_h = (c - h)$, $\sigma_\theta = 0$. Therefore, $r \geq r_h$, $\sigma_\theta \geq 0$, yields tensile stress. Here, c is the outer radius of the thick shell and h is the distance from the outer wall.

Taylor et al. [16] studied the problem of broken cylindrical shell based on high-speed photographic records and concluded the axial crack first appeared in the outer wall, which gradually widened with the expansion of the shell. Then, the crack penetrated the inner wall and made the shell break until the tube diameter expanded to twice its original size. Therefore, the shell breaks in the condition where the compressive stress zone of σ_θ disappears and the crack penetrates the inner wall.

Eq. (16) shows that the position of interface rb is h when σ_θ changes from tensile stress to compressive stress. This can occur when $\sigma_\theta = 0$, as follows:

$$0 = -P_2 + 1.15\sigma_Y^D\left(1 + ln\frac{c - h}{b}\right) +$$
$$\rho\left[\left(u_b^2 + b\frac{du_b}{dt}\right)ln\frac{c - h}{b} - \frac{u_b^2}{2}\left(1 - \frac{b^2}{(c-h)^2}\right)\right] \tag{19}$$

The condition that the area of compressive stress disappears is h=c-b; thus, the tubular shell is broken only when the value of P_b drops to the value of 1.15 σ_Y^D overtime.

Then, r=c and $\sigma_r = -P_1$ for the outer wall of the shell, substituting them into Eq. (15). The expression of the velocity of the particle on inner wall variation with time is obtained as follows:

$$\frac{d(u_b)}{dt} = \frac{p_2 - p_1 - 1.15\sigma_Y^D ln\frac{c}{b}}{\rho bln\frac{c}{b}} - \frac{u_b^2}{b}\left(1 - \frac{1 - \frac{b^2}{c^2}}{2ln\frac{c}{b}}\right) \tag{20}$$

The motion process of the shell can be tracked by Eq. (20), and the whole process of the shell expansion can be recorded. Then, the initial flying speed can be obtained by Eq. (20) when the shell is broken.

2.2 Liquid Ring Rupture Model

Before the shell breaks, the fuel ring (particles layer) moves outwards under the driving pressure of the detonation product of the center dispersal charge. It is also constrained by the shell. After the shell breaks, the fuel ring is governed by the detonation product of the center dispersal charge, and the size, speed, route, and interaction with particles of shell fragments during dispersal are complex and have less affect on the dispersion of the particles. Therefore, the present study mainly focuses on dispersal particles rather than on the lethality of shell fragments. It is assumed that the effect of the shell fragments on the fuel is ignored after the shell is broken. Therefore, after the shell breaks the fuel ring is directly affected by the external air resistance and the driving force of the explosive product of the center dispersal charge, as shown in Figure 4.

The fuel ring expands outward under the action of the center dispersal charge, and the shell bursts after a certain time because of the constraints in the early stage of the outer shell. The propagation of the stress wave is reversed a few times and tends to be balanced; thus, the effect of the
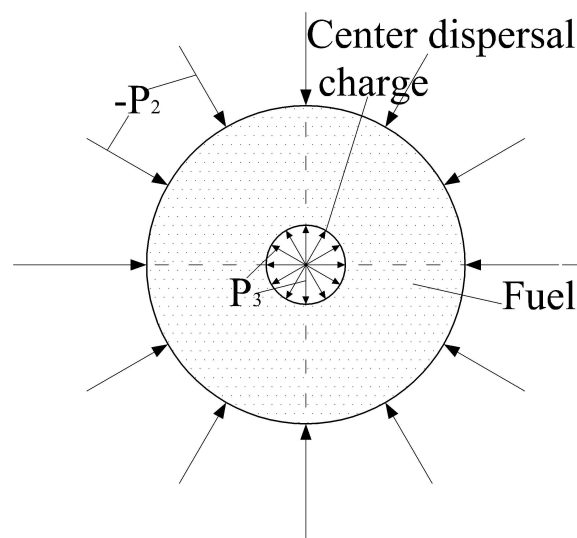

Figure 4. The stress state of the fuel ring. (P_3 is the driving pressure of the detonation product of the center dispersal charge; $-P_2$ is the constraining force of the shell.)

stress wave in the model is ignored. The destruction process of the fuel ring is similar to that of the shell and the fuel compressed by shock waves is considered an incompressible medium similar to the case of the shell rupture model.

The radius of the fuel ring is a, and the outer radius is b. Thus, the following equation is obtained:

$$\sigma_{rf} = -p_3 + 1.15\sigma_{Yf}^D ln\frac{r}{a} +$$
$$\rho\left[\left(u_a^2 + a\frac{du_a}{dt}\right)ln\frac{r}{a} - \frac{u_a^2}{2}\left(1 - \frac{a^2}{r^2}\right)\right] \quad (21)$$

The other two principal stresses can be obtained by substituting Eq. (7) and the plane strain condition:

$$\sigma_{\theta f} = -p_3 + 1.15\sigma_{Yf}^D\left(1 + ln\frac{r}{a}\right) +$$
$$\rho\left[\left(u_a^2 + a\frac{du_a}{dt}\right)ln\frac{r}{a} - \frac{u_a^2}{2}\left(1 - \frac{a^2}{r^2}\right)\right] \quad (22)$$

$$\sigma_{zf} = -p_3 + 1.15\sigma_{Yf}^D\left(\frac{1}{2} + ln\frac{r}{a}\right) +$$
$$\rho\left[\left(u_a^2 + a\frac{du_a}{dt}\right)ln\frac{r}{a} - \frac{u_a^2}{2}\left(1 - \frac{a^2}{r^2}\right)\right] \quad (23)$$

Eq. (21), (22), and (23) are the stress distributions inside the fuel ring at different radii. In general, the pressure on the inner wall is much greater than the yield stress of the fuel. Unless P_3 is reduced to the value of σ_{Yf}^D or even lower, the inner wall of the fuel ring is in a compressive state:

$$\sigma_r|_a = -p_3, \sigma_\theta|_a = -p_3 + 1.15\sigma_{Yf}^D \quad (24)$$

As r increases, the compressive stress value of $\sigma_{\theta f}$ decreased with P_3, as shown in Eq. (22). Suppose $r_{hf} = (b - h)$, $\sigma_{\theta f} = 0$; so $r > r_h$, $\sigma_{\theta f} \geq 0$; here, $\sigma_{\theta f}$ is the tensile stress, b is the outer radius of the fuel ring, and h is the distance from the outer radius of the fuel ring. By Eq. (22), the position of the interface that is the value of h, where $\sigma_{\theta f}$ changes from tensile stress to compressive stress can be obtained, which can be given under the condition of $\sigma_\theta = 0$, as shown in Eq. (25):

$$0 = -p_3 + 1.15\sigma_Y^D\left(1 + ln\frac{c - h}{b}\right) +$$
$$\rho\left[\left(u_b^2 + b\frac{du_b}{dt}\right)ln\frac{c - h}{b} - \frac{u_b^2}{2}\left(1 - \frac{b^2}{(c - h)^2}\right)\right] \quad (25)$$

The condition where the area of compressive stress $\sigma_{\theta f}$ disappears is h = b–a; thus, the tubular fuel ring can be broken only when the value of P_3 drops to 1.15 σ_{Yf}^D overtime. The expression of the velocity of the particle on the inner

wall changing with time is obtained by using Eq. (21) with r = b and $\sigma_r = -P_2$ for the outer radius of the fuel ring.

$$\frac{du_a}{dt} = \frac{p_3 - p_2 - 1.15\sigma_{Yf}^D ln\frac{b}{a}}{\rho aln\frac{b}{a}} -$$
$$\frac{u_a^2}{a}\left(1 - \frac{1 - \frac{a^2}{b}}{2ln\frac{b}{a}}\right) \quad (26)$$

The motion of the fuel ring can be tracked. The whole expansion process of the fuel ring can also be recorded. The thickness and speed of the fuel ring can be obtained by Eq. (26) with the assumption the number of particles does not change. Milne et al. concluded that the width of the initial fragments correlates with the thickness of the compacted layer, and the numbers of fragments are very similar at early and late times [17]. As an approximation, the thickness of the fuel ring was considered the maximum size of the initial fragments in the present study.

2.3 Fuel Block Secondary Crushing Model

The fuel blocks formed by the initial fragmentation move and interact with air. Under the action of air resistance, the fuel blocks undergo a secondary crushing process. By ignoring the collisions between fuel blocks, the main consideration is the fuel block and the air effect. Under the action of air, the main effects of fuel block are pneumatic stripping and fuel evaporation atomization. If we suppose that the fuel block is spherical, the characteristic scale of the fuel block is its average radius. The stripping model and evaporation model are then used to describe the stripping and evaporation of the fuel block.

2.3.1 The Peeling Effect Model

The stripping effect of a fuel block or droplet is mainly caused by the friction resulting from the relative motion of air and fuel block or droplet, and the stripping rate can be expressed by Eq. (27) according to Engel [18]. In this model, the surface of the droplet starts to peel off due to the convective shear action caused by the very fast flow of the gas. Therefore, the droplet is gradually shattered, and its radius keeps diminishing.

$$\frac{dl}{dt} = -\left(\frac{\rho\mu}{\rho_L^{ini}\mu_L}\right)^{1/6}\left(\frac{\mu_L}{\rho_L^{ini}}\right)^{1/2}|u - u_L|^{1/2}l^{-1/2} \quad (27)$$

where ρ and ρ_L^{ini} are the densities of the air and fuel medium, respectively; μ and μ_L are the viscosity coefficients of the air and fuel medium, respectively; u and u_L are the speed of the air and fuel medium, respectively; and l is the average radius of the fuel particle or droplet.

2.3.2 The Evaporation Effect Model

Fuel particles or droplets keep moving in the air. Because of temperature differences between air and fuel particles or liquid droplets, heat exchange between air and fuel particles or droplets causes fuel particle or droplet evaporation. According to the Eidelman evaporation model [19], it is shown as Eq. (28). In the model, it is assumed that the whole surface of the droplet evaporates evenly, and the temperature of the droplet remains constant during evaporation.

$$\frac{dl}{dt} = -\frac{3k_{GAS}N_u(T - T_L)}{\pi l \rho_L^{ini} L} \tag{28}$$

where ρ_l^{ini} is the density of fuel particles or droplets, k_{GAS} is the heat conductivity of air, N_u is the Nusselt number, and T $/T_l$ is the temperature of air/ temperature of the fuel particle or droplet (K).

2.3.3 Variation of the Fuel Secondary Crushing Scale

The variation of the fuel secondary crushing scale can be obtained by combining the stripping effect and evaporation effect [19], where the size of the changed fuel particle or droplet is the sum of Eq. (27) and Eq. (28):

$$\delta = \frac{9k_{GAS}N_u(T - T_L)}{\pi l^2 \rho_L^{ini} L} +$$
$$3\left(\frac{\rho\mu}{\rho_L^{ini}\mu_L}\right)^{1/6}\left(\frac{\mu_L}{\rho_L^{ini}}\right)^{1/2}|u - u_L|^{1/2}l^{-3/2} \tag{29}$$

Among them: δ is the variable related to the reduction (1/s) of droplet size. The particle diameter is calculated by Eq. (30), where a_1 is the initial inner radius of the fuel ring, b_1 is the initial outer radius, d_1 is the particle initial diameter, and d is the particle diameter.

$$\begin{cases} a = a_1 + u_a \cdot t \\ b = \sqrt{b_1^2 - a_1^2 - a^2} \\ d_1 = b - a \\ d = d_1 + \delta \cdot t \end{cases} \tag{30}$$

In the model, the minimum size of particles d_{min} is determined for the particles or drops that do not break up or decrease further. According to Hinze's suggestion [20], the droplet size was determined by the turbulent kinetic energy around the droplet. The droplet will break down into smaller droplets in the condition of the pressure fluctuation caused by the changes in velocity is greater than the surface tension between the two phases in the droplet size range. In the dilute

solution, the droplet interaction and droplet coalescence are not considered. The minimum size of the particles is shown:

$$d_{min} = 6.2 \cdot \left(\frac{\rho_L^{ini}}{\rho}\right)^{\frac{1}{4}} \cdot \left(\frac{\mu_L}{\rho_L^{ini} \cdot 0.5 \cdot d_1 \cdot u_{L1}}\right)^{\frac{1}{2}} \cdot d_1 \tag{31}$$

In Eq. (31), u_{L1} is the initial velocity of the particle. μ_L is the viscosity coefficient of the dispersal material.

2.4 Particle or Droplet Motion Model

The motion of fuel particles or droplets can be modeled by single-particle motion dynamics to simplify the model and calculate the motion quickly when the collisions between fuel particles or droplets are ignored. In the single-particle dynamics model, the effect of the relative continuous phase fluid particles is not considered, and the interaction between particles and particle fluctuating is not considered. This model is a one-way coupling model, in which only the force and movement of a single particle in the continuous phase fluid is considered.

In addition, the particle group resistance coefficient was considered by assuming that if more than one particle in the flow field, there are interactions between the particles, such as direct collisions between particles and interaction effects caused by the wake of particles.

Corrsin and Lumley suggested the pressure gradient of the flow introduced by the field inhomogeneity in space-time in the turbulence field was important for particle translation [21]. Maxey and Riley proposed the equation of particle motion and considered the forces on a particle in the nonuniform flow; the Faxen correction for unsteady Stokes flow was derived [22]. Cen and Fan analyzed the stress of coal particles in gas flow and concluded the coal particles rotated at high speed to produce lift effect [23].

According to the above, the equation of single-particle motion in the Lagrange coordinate system is as follows:

$$\begin{aligned} m_p \frac{du_p}{dt} &= \sum F \\ &= F_d + F_m + F_p + F_B + F_M + F_s + F_f \\ &= \frac{1}{8}\rho_p\pi d_p^2 C_d |u_f - u_p|(u_f - u_p) + \\ &\quad \frac{\pi d_p^3}{12}\rho_p\frac{d}{dt}(u_f - u_p) - \frac{\pi d_p^3\rho_f}{6}\frac{du_f}{dt} \\ &\quad + \frac{3}{2}(\pi\rho_p\mu)^{\frac{1}{2}}d_p^2\int_{-\infty}^{t}\frac{d}{dt}(u_f - u_p)(\tau - t)^{-\frac{1}{2}}d\tau + \\ &\quad \frac{1}{8}\pi d^3\rho_f(u_f - u_p)w + 1.61(\mu_f\rho_f)^{\frac{1}{2}} \\ &\quad d_p(u_f - u_p)\left|\frac{du_f}{dy}\right|^{\frac{1}{2}} + (m_p - m_f)g \end{aligned} \tag{32}$$

A Whole Explosive Dispersion Process Prediction Model for Fuel Clouds

In Eq. (32), F_d is the resistance of particle motion, F_m is the additional mass force, F_p is the pressure gradient force, F_B is the Basset force [24], F_M is the Magnus force and F_s is the Saffman force [25]. Elghobashi and Truesdell concluded that the buoyancy and drag forces took the main effect in the gravity direction [26]. Meanwhile, the drag and Basset forces were the main forces in the lateral directions where the Basset force was at the lowest order of magnitude lower than the drag. Here ρ_f and ρ_p are the densities of the air and particle, respectively; μ_f are the viscosity coefficients of the air; u_f and u_p are the velocity of the fluid and particle respectively, and dp is the average radius of the fuel particle or droplet; w is the rotational velocity of the particle. Therefore only drag and gravity are considered here because the others are more complicated and have smaller effects. In addition, ignoring the other forces simplifies and more quickly calculates the general form of the single-particle motion.

2.4.1 Drag Force and Drag Coefficient of a Flow Field

In the problem of explosion disperse particles, the drag force of flow field plays an important role in the movement of particles when the particle flow gradually transforms from dense flow into sparse flow. Compared with the drag force of the flow field, the interaction force between particles is smaller and more complicated. Consequently, it is neglected here. A modified particle group resistance coefficient was raised as a supplement in § 2.4.2 in this paper. The expression of resistance F_d is written as Eq. (33) according to the aerodynamic drag force equation proposed by Borisov [27].

$$F_d = C_d \frac{1}{2} \rho_f |u_f - u_p| (u_f - u_p) S \tag{33}$$

where, u_f and ρ_f are the fluid velocity and density, respectively, u_p is the speed of the particles, S is the windward area of the particles, $S = \pi r^2$, and C_d is the drag coefficient.

In theory, the drag coefficient can be obtained from the Navier-Stokes equation. However, the surface layer of spherical particles is very complicated. At present, the resistance coefficient depends mainly on the experiment. The resistance coefficient of particles is closely related to the Reynolds number of the particles. As a result, the calculation formula of the Reynolds number of the particles is as follows:

$$Re = \frac{d_p \rho_f}{\mu} |u_f - u_p| \tag{34}$$

where, $\frac{\mu}{\mu_0} = \left(\frac{T_f}{T_0}\right)^{0.77}$ and $\mu_0 = 1.71 \cdot 10^{-5} kg/(m \cdot s)$ is assumed.

Clift et al. summarized and analyzed the theoretical research and experimental data for different Reynolds number intervals [28]. And the empirical formula of drag coefficient suitable for piecewise expression over a larger Reynolds number range is recommended. Here the drag coefficient is calculated using the simple expression suggested by Schiller and Naumann [29]:

$$C_D = \begin{cases} \frac{24}{Re}(1 + 0.15 Re^{0.687}) & Re < 1000 \\ 0.44 & Re \geq 1000 \end{cases} \tag{35}$$

2.4.2 Modification of Particle Group Resistance Coefficient

If there are multiple particles in the flow field, there are interactions between the particles, and one of the interactions is direct collisions between particles. Another interaction is achieved through the wake of particles. Therefore, even if the particle concentration is very low, there is significant interaction. The resistance of particles received is significantly affected by the indirect action of the fluid. For the drag coefficient of the particle group, according to the equation proposed by Wen and Yu [30], the calculation method is the product of the drag coefficient of a single particle and the function of a particle volume fraction:

$$C_D = C_{DS} F(\alpha) \tag{36}$$

The expression of volume fraction is $F(\alpha) = \alpha^{-4.7}$. Here, α is the void fraction. Combined with the drag coefficient of the single particle, the drag coefficient of the particle group can be expressed as:

$$C_D = \begin{cases} \frac{24}{Re}(1 + 0.15 Re^{0.687}) \cdot \alpha^{-4.7} & Re < 1000 \\ 0.44 & Re \geq 1000 \end{cases} \tag{37}$$

2.5 The Expansion Model of Center Tube Detonation Product

The expansion law of detonation products conforms to the polytrophic exponential equation of state: $pv^r =$ const. Here, p is the pressure of detonation product, which is proportional to $r^{-3\gamma}$, v is the specific volume of detonation product, which is proportional to r^3, γ is the polytrophic exponent, and r is the expansion radius of the detonation product. In addition, the equation can be changed to the following:

$$\frac{p}{p_0}\left(\frac{v_0}{v}\right)^\gamma = \left(\frac{a_0}{a}\right)^{2\gamma} \tag{38}$$

In Eq. (38), p and v are the pressure and volume of detonation products in the process of expansion, respectively, p_0 and v_0 are the pressure and volume of the detonation products for the instantaneous detonation, respectively, γ is the index of detonation products, which is approximately equal to 3, and a_0 is the radius of the center tube before expansion.

2.6 The Axial Expansion Effect Correction Model

The practical dispersal structure is a finite length cylindrical form. The detonation process is affected by the rarefaction wave of an axis because dispersal center charge is detonated in different ways. Therefore, the impulse working on the fuel and shell is different, which results in the change of the initial velocities both the fuel particle or droplet and debris of the shell. The sparse wave propagates inside and follows the detonation wave after the dispersal center is detonated, decreasing the impulse of the detonation product work on the inner surface of the fuel. Therefore, the velocity near the detonated decreases and the initial velocity can be estimated by Eq. (39) based on the different detonate distances:

$$v_x = v_0\left(\frac{i_x}{i_0}\right) \tag{39}$$

where, v_0 is the maximum velocity, v_x is the micro velocity in the point x, i_0 is the largest impulse applied on the inside wall of fuel ring, and i_x is the impulse of the inside wall of the fuel ring at point x.

The particles and debris form after the fuel ring and shell break, and the speed along the axial distribution are actually caused by the impulse that is applied to the inside wall and changes with the length along the axial structure.

The parameter $\alpha = x/L$ is introduced, where x is the distance from the initiation point along the axis and L is the length of the central tube charge. When one end of the central tube dispersal charge structure detonates, the impulse at a different section can be determined according to the equation suggested by Zhang et al. [31]. It is applied to the openings on both ends as the expression of Eq. (40).

$$i_x = \frac{i_0}{8}\left\{\begin{array}{l} 1 + 6\alpha(1-\alpha) + \frac{3\alpha}{2}ln\left[\frac{1}{a}(3-2\alpha)\right] \\ +6\alpha(1-\alpha)(2\alpha-1)ln\frac{3-2\alpha}{2(1-\alpha)} \end{array}\right\} \tag{40}$$

Then, by calculating using Eq. (40):

$$\alpha = 0, \ i_x = 0.125i_0; \ \alpha = \frac{1}{4}, \ i_x = 0.503i_0 \ ; \ \alpha = \frac{1}{2},$$

$$+6\alpha(1-\alpha)(2\alpha-1)ln\frac{3-2\alpha}{2(1-\alpha)}$$

When one end of the tube is open and another is closed the Eq. (41) is obtained.

$$i_x = \frac{i_0}{8}\left\{\begin{array}{l} \frac{8-\alpha^3}{(1.7-\alpha)^2 \times 2.025} - \frac{3\alpha^2}{(1.7-\alpha)\times 1.42} + \\ \frac{3\alpha}{2}ln\left[\frac{1.42}{\alpha}(1.7-\alpha)\right] + \frac{15\alpha}{4} + \frac{1.42(1.7-\alpha)}{4} \end{array}\right\} \tag{41}$$

Then, calculating yields the following:

$$\alpha = 0, \ i_x = 0.246i_0 \ ; \ \alpha = \frac{1}{4}, i_x = 0.503i_0; \ \alpha = \frac{1}{2},$$

$$i_x = 0.685i_0 \ \alpha = \frac{3}{4}, \ i_x = 0.838i_0; \ \alpha = 1, \ i_x = i_0$$

The six models presented constitute the theory analysis model of a fuel cloud during explosive dispersal. The fuel ring can be divided into units (droplets or particles) along the axial direction. The characteristics of the units such as displacement, velocity, and particle size can then be calculated. Therefore, cloud contour can be obtained by the units.

3 Results and Discussion

In the present study, four cases were predicted by the model for static fuel dispersal and dynamic fuel dispersal. The process of fuel dispersal and cloud morphology characteristics including cloud radius, cloud velocity, and particle size were calculated, and among those characteristics, cloud radius and cloud velocity were selected to validate the proposed model. An experiment was performed to support the proposed model. The other experimental data adopted from previous studies [32–34] were also used to validate the model because of the high cost, difficulty, and complexity of the experiment. The accuracy of the model was tested by comparing experimental results to those obtained by the model.

3.1 Static Initial Condition for Fuel Dispersal of Case 1

3.1.1 The Prediction Model for Static Fuel Dispersal

The characteristics of static dispersal were predicted by the model and the initial conditions for the calculation are presented in Table 1.

Figure 5 shows that the radius of the cloud initially increases with time. Then, the radius gradually becomes a constant value after 100 ms. The height of the cloud increases during this phase.

Figure 6 shows the diameter, velocity and droplet size changing with time, where the maximum diameter of the cloud is 7.23 m and the initial velocity is approximately 537 m s^{-1}. The figure also shows that the velocity of the

Table 1. The initial conditions for case 1 (the static explosive dispersal of 10 kg fuel).

		Initial conditions for calculation
Shell	Diameter	200 mm
	Height	400 mm
	Thickness of Shell	2 mm
	Material Density	7800 kg m^{-3}
	Tensile Strength	235 MPa
Fuel	Taterial Density	800 kg m^{-3}
	Tensile Strength	0.1 MPa
	Viscosity Coefficient	0.01 Pa s
Center Charge	Diameter	20 mm
	Height	400 mm
	Density	1500 kg m^{-3}
	Detonation Pressure	15 GPa
	Initial Multiple Index of Detonation Product	3.0
Air	Initial Pressure	0.1 MPa
	Density	1.225 kg m^{-3}
	Viscosity Coefficient	1.8e–5 Pa s
	Sound Velocity	340 ms^{-1}

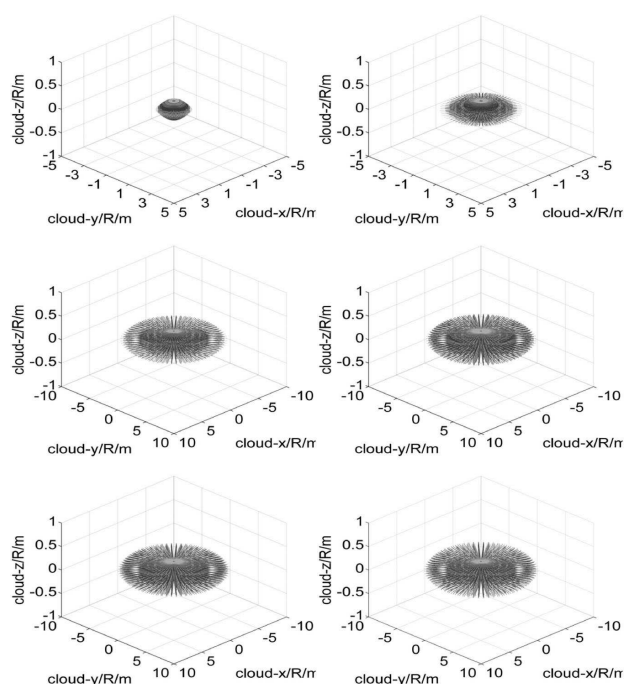**Figure 5.** The process of static explosive dispersal of 10 kg fuel (t = 2 ms, 5 ms, 25 ms, 50 ms, 100 ms, 200 ms)

Figure 6. The characteristics of static explosive dispersal of 10 kg fuel (a) The velocity curve of the static explosive dispersal cloud changing with time. (b) The curve of the median droplet size changing with time. (c) The maximum radius curve of the cloud changing with time in the radial direction. (d) The droplet's size of 134 kg fuel distributed changing with cloud radius under the initial static condition at different times.

particle size reduced at the joint action of the evaporation effect and stripping effect, the particle radius and speed were smaller, decreasing the resistance. Therefore, the velocity slowed in the second stage. Because of the minimum particle size in the model, particles did not break up or decrease after reaching the minimum. Then, the particle size reached a minimum value which could no longer continue to be broken up to reduce the resistance. In the third stage, speed decreased sharply in a short time until the speed significantly decreased. Followed by the speed, the resistance greatly reduced. At the last stage, the deceleration was reduced to a smaller value. The diameter of the cloud nearly stopped increasing at this stage. The speed decreased slowly until it reached a speed of 0 and deceleration of 0, and the diameter of the cloud remained the same.

Figure 6 shows the relationship between particle size distribution, displacement, and time. The initial dispersed droplet diameter is 0.006 m. As time increased, the particles were further broken, constantly reducing the particle size. The small particles were dispersed farther in the radial direction because the small size droplets had a larger initial velocity. Moreover, most of the droplet size reached a minimum of 50 ms.

3.1.2 Comparison with Experiments of Static Fuel Dispersal

An experiment of static fuel dispersion was conducted in the field to validate the proposed model. The dispersal device was a center tubular structure with dimensions of 200 mm×400 mm. The shell was made of steel material

cloud demonstrated four different stages. At first, the velocity dropped rapidly, then, it decreased slowly and dropped rapidly again in the third stage, flattening out in the last stage. The reason was in the early stage, the particles gained larger initial speed because of the large driving force of the center charge, increasing the resistance. At this time, the speed of particles quickly decelerated. When the
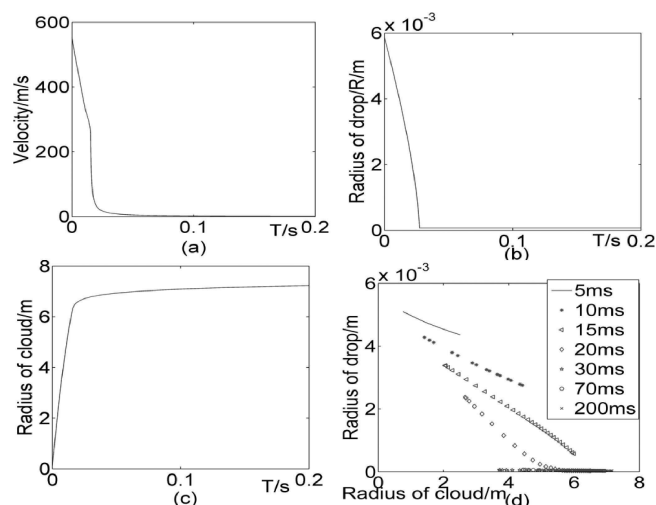
with a thickness of 2 mm; the center charge was TNT with dimensions of 20 mm×400 mm and a density of 1500 kg m^{-3}. The ratio of center charge to fuel was approximately 2%. The total mass of dispersal fuel was 10 kg and its density was 800 kg m^{-3}. The photographing frequency was 2000 frames per second and the resolution ratio of each photo was 1280×800. The cloud formed during fuel dispersion is shown in Figure 7. The fuel dispersing process was recorded by a high-speed camera. The experimental results were compared with the simulation results, as shown in Tables 2–3.

The Tables 2–3 show that the cloud diameter and the speed of fuel particles are consistent with the experimental results. The cloud development by the model (Figure 5) is very similar to the explosive dispersal experiment (Figure 7). In addition, the characters such as cloud radius, velocity, and particle size can be calculated by the model before the test, which is very valuable in fuel dispersal research.

3.2 Static Initial Condition for Fuel Dispersal of Case 2

3.2.1 The Prediction Model for Fuel Dispersal

The characteristics of the static disperse cloud were calculated and analyzed. The initial conditions for the calculation were shown in Table 4.

Figure 8 shows the developmental process of the static dispersal cloud at different times. The cloud was basically stable after 100 ms and the cloud shows a flat cylinder shape.

Figure 9 shows the diameter, velocity, and droplet size-changing curve of the dispersal cloud. The figure shows that the maximum diameter of the cloud was 12 m, the initial velocity was 300 m s^{-1}, and the initial droplet size was 0.015 m. The droplet size decreases over time. Small particles were on the outer edge of the cloud in the radial direction, whereas the bigger particles were on the inner edge in the radial direction before 70 ms in Figure 9-d.

Figure 7. The cylindrical static explosive dispersal of 10 kg fuel (t = 2 ms, 5 ms, 25 ms, 50 ms, 100 ms, 200 ms).

Table 2. Comparison of the cloud radius parameters for the experiment date and simulation date.

Series code	The fuel density kg m^{-3}	Cloud radius (m) at different times (ms)							
		10	20	30	50	75	100	150	200
Experiment group	800	3.72	5.20	5.96	6.28	6.67	7.01	7.18	7.36
Simulation group	800	4.47	5.91	6.56	6.92	7.02	7.09	7.17	7.23
Error rate (%)		20.16	13.65	10.07	10.19	5.25	1.14	−0.14	−1.77

Table 3. Comparison of the cloud velocity parameters for the experiment date and simulation date.

Series code	The fuel density kg m^{-3}	Cloud velocity (m/s) at different times (ms)				
		2	5	10	12	15
Experiment group	800	519.3	461.6	387.9	346.2	288.5
Simulation group	800	507.1	450.2	351.2	318.5	273.1
Error rate (%)		−2.34	−2.47	−9.46	−8.00	−5.34

A Whole Explosive Dispersion Process Prediction Model for Fuel Clouds

Table 4. The initial conditions for case 2 (the static explosive dispersal of 116 kg water).

Initial conditions for calculation		
Shell	Diameter	300 mm
	Height	1650 mm
	Thickness of Shell	2 mm
	Material Density	2700 kg m^{-3}
	Tensile Strength	100 MPa
Fuel	Material Density	1000 kg m^{-3}
	Tensile Strength	0.1 MPa
	Viscosity Voefficient	0.001 Pa s
Center charge	Diameter	25.4 mm
	Height	1310 mm
	Density	1500 kg m^{-3}
	Detonation Pressure	10 GPa
	Initial Multiple Index of Detonation Product	3.0
Air	Initial Pressure	0.1 MPa
	Density	1.225 kg m^{-3}
	Viscosity Coefficient	1.8e−5 Pa s
	Sound Velocity	340 m s^{-1}

Figure 9. The characteristics of the static explosive dispersal of 116 kg water (a) The maximum radius curve of the static explosive dispersal cloud changing with time in the radial direction. (b) The velocity curve of the cloud changing with time. (c) The curve of the median droplet size changing with time. (d) The droplet's size-changing with cloud radius under the initial static condition at different times.

Figure 8. The process of static explosive dispersal of 116 kg water (t = 2 ms, 5 ms, 25 ms, 50 ms, 100 ms, 200 ms).

3.2.2 Comparison with Experiments of the Static Dispersal Experiment

A cylindrical explosive dispersal experiment of 116 kg water was performed [32]. The water was in a thin-walled aluminum cylindrical container with a length of 1.65 m and an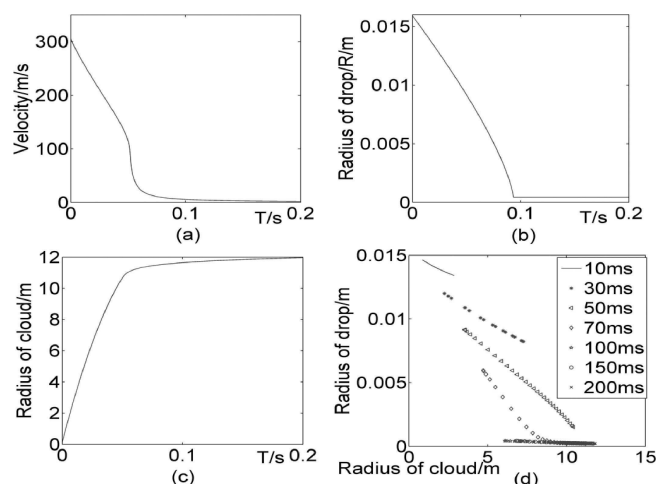 inner diameter of 30 cm. The water was dispersed by a 1 kg central cylindrical explosive charge, which was in a 25.4 mm internal diameter thin-walled steel tube. A high-speed camera (2,000 frames s^{-1}) was used to measure the dispersal of gasoline.

The results in Table 5 show that the cloud profile and the initial speed of the fuel particles are consistent with the experimental results. Moreover, the static cloud development of Figure 8 is similar to the test of explosive dispersal showed in Figure 10 [32].

3.3 Dynamic Initial Condition for Fuel Dispersal

3.3.1 The Case of Dynamic Fuel Dispersal

The characteristics of static dispersal cloud were calculated and analyzed, and the initial calculation conditions were shown in Table 6.

The dynamic cloud was analyzed under 0.12 Mach number (40 m s^{-1}) falling speed conditions. The initial conditions

Table 5. The comparison of the experiment results and the simulation results for water 116 kg

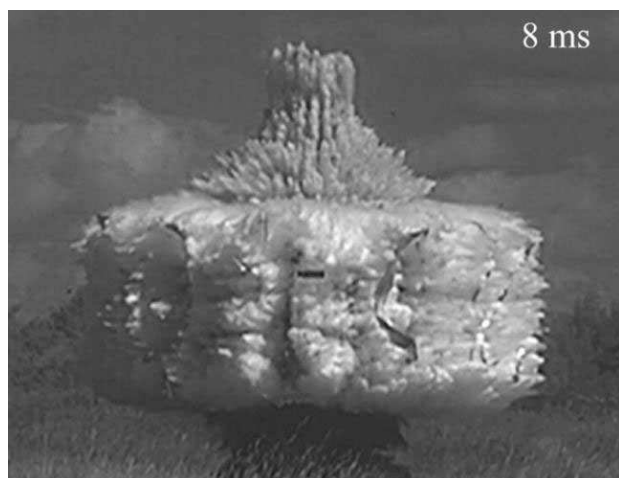| M/C (The mass ratio of fuel to explosive charge)	Initial velocity (m s^{-1}) 116
Experiment group	300
Simulation group	304
Error rate (%)	−1.31

Figure 10. Cylindrical explosive dispersal of 116 kg water [32].

Table 6. Initial conditions for the case of the dynamic explosive dispersal of 125 kg solid-liquid mixed fuel

		Initial conditions for calculation
Shell	Diameter	370 mm
	Height	1150 mm
	Thickness of Shell	3 mm
	Material Density	7800 kg m^{-3}
	Tensile Strength	235 MPa
Fuel	Material Density	1000 kg m^{-3}
	Tensile Strength	0.1 MPa
	Viscosity Coefficient	0.0075 Pa s
Center Charge	Diameter	28 mm
	Height	1150 mm
	Density	1560 kg m^{-3}
	Detonation Pressure	21 GPa
	Initial Multiple Index of Detonation Product	3.0
Air	Initial Pressure	0.1 MPa
	Density	1.225 kg m^{-3}
	Viscosity Coefficient	1.8e−5 Pa s
	Sound Velocity	340 m s^{-1}
Fuel Dispersal	Falling Speed	40 m s^{-1}

Figure 11. The process of dynamic explosive dispersal of 125 kg solid-liquid mixed fuel with a falling speed of 0.12 Mach number (40 m s^{-1}) (t = 2 ms, 5 ms, 25 ms, 50 ms, 100 ms, 200 ms).

Figure 12. The characteristics of dynamic explosive dispersal of 125 kg solid-liquid mixed fuel with a falling speed of 0.12 Mach number (40 m s^{-1}) (a) The velocity curve of explosive dispersal cloud edge with a falling speed of 0.12 Mach number. (b) The curve of median droplet size changing with time at falling speed of 0.12 Mach number. (c) The maximum radius curve of explosive dispersal cloud over time in the radial direction with a falling speed of 0.12 Mach number. (d) The droplet's size of fuel distributed changing with cloud radius at different times with a falling speed of 0.12 Mach number.

in Table 6 were set as the same as those for the dynamic experiment [33].

Figure 11 shows that the cloud was basically stable in the radial direction after 100 ms. Figure 12 shows the displacement, velocity and particle size curve of the cloud; the falling speed was 0 Mach number, and the other initial conditions were set as the same as those of the dynamic conditions. In order to compare the changes after adding the falling velocity, a case of static fuel dispersal was predicted by the model.

For contrast of the characteristics of the dynamic dispersal and static dispersal, Figure 13 shows the characteristics of static explosive dispersal of 125 kg solid-liquid mixed fuel. The other initial conditions were set as the same
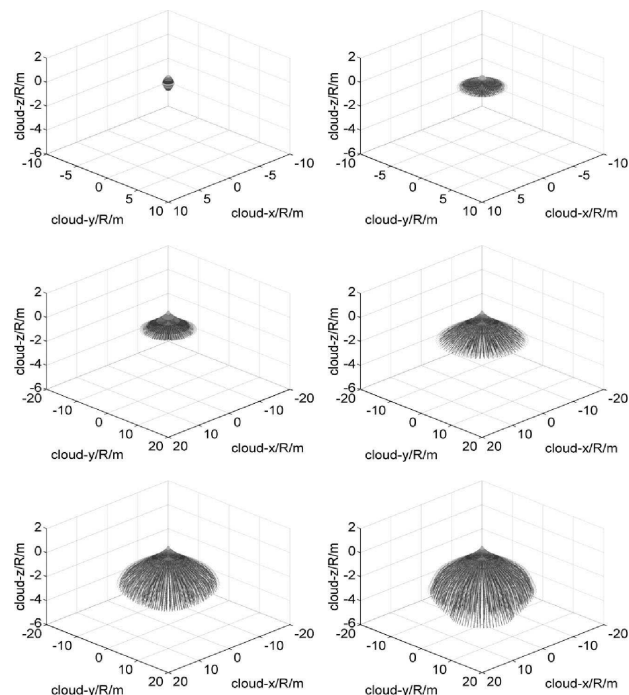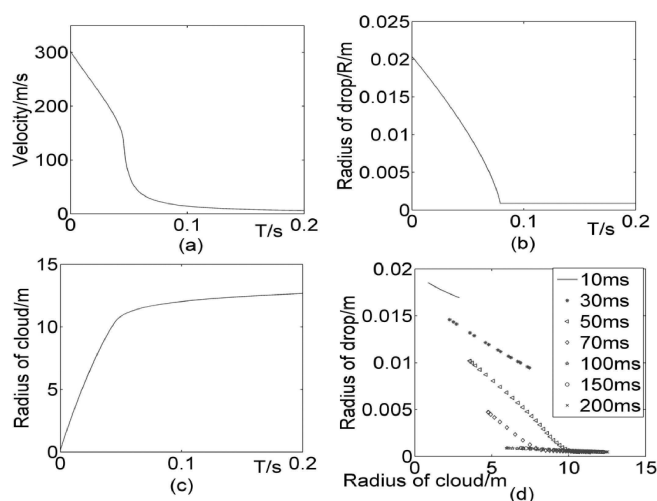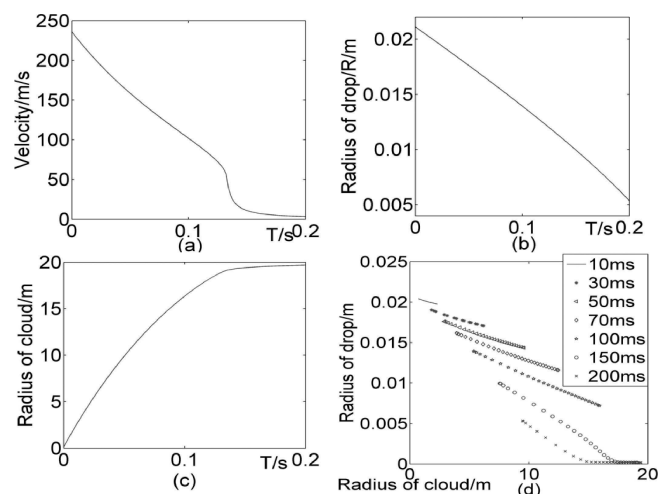
A Whole Explosive Dispersion Process Prediction Model for Fuel Clouds

Figure 13. The characteristics of static explosive dispersal of 125 kg solid-liquid mixed fuel. (a) The velocity curve of static explosive dispersal cloud edge (b) The curve of median droplet size changing with time. (c) The maximum radius curve of static explosive dispersal cloud over time in the radial direction. (d) The droplets size of fuel distributed changing with cloud radius at different times.

Figure 14. The dynamic fuel dispersal cloud [34].

as in Table 6. Figures 12 and 13 show that adding the fall velocity, compared with the static initial dispersal, the radius of the cloud decreased from 19 m to 12.5 m and the initial median droplet size decreased from 0.021 m to 0.0203 m. In contrast, the height of the cloud increased from 1.2 m to 6 m, the initial velocity increased from 240 m s^{-1} to 300 m s^{-1}. Similar to the initial static dispersal, the small particles were dispersed farther in the radial direction because of the larger initial velocity than the big particles. Then, small particles experienced large resistance because of the high initial velocity, so the velocity quickly decreased.

However, large particles have large inertia and small resistance because of the big mass and small initial velocity. Thus, the velocity of big particles slowly decreased. Moreover, adding falling speed, particles experienced larger air resistance in the axial direction, promoting the breakage of the particles. Then, particles broke up faster, causing greater resistance and shorter flight time for the particles. Therefore, the cloud radius decreased in the radial direction and

moved further in the axial direction. At the same time, the median particles broke up to a minimum size at 78 ms, while in the initial static dispersal rate, the median particles broke up to a minimum size after 200 ms. Thus, the condition of dynamic dispersal is more effective than the static initial state.

The morphology of the dynamic simulated cloud with a Mach number of 0.12 in Figure 10 is an "umbrella shape" and is very similar to the actual FAE cloud shown in Figure 14 [34]. Moreover, a hollow area in the clouds appears, making the appearance of the simulated cloud correspond to the experimental results.

3.3.2 Experiment of Dynamic Fuel Dispersal

Wang et al. [33] performed a dynamic cloud formation experiment to the study of dispersal and detonation field characteristics using a cylindrical shell. The cylinder size was 370 mm × 1150 mm, filled with 125 kg solid-liquid mixed fuel. The center charge was 1.08 kg TNT and the detonation height of the fuse was 2 m. The device landed at falling speed of 40 m s^{-1}. The test adopted the hot air ball method to drop the dynamic cloud detonation device. After the hot air balloon reached a height of 300 m, the dynamic cloud detonation device was released to form the endpoint dynamic cloud dispersal and detonation process. Table 7 shows that the radii of cloud at different times in the radial

Table 7. Comparison of the cloud radius parameters for the dynamic experiment.

Series Code	Diameter of Center Charge			Cloud Radius/(m) at Different Times/(ms)				
	$\emptyset$/m	5	25	50	100	125	150	200
Experiment Group	28	3.6	6.9	9.0	9.8	10.2	11.0	11.9
Simulation Group	28	3.5	6.7	10.8	12.0	12.2	12.4	12.6
Error Rate (%)		−2.78	−2.90	20.00	22.45	17.65	12.73	5.88

direction obtained by the model are consistent with that obtained from the actual experiment, and Figure 14 [34].is similar to Figure 11 obtained by the model, indicating that the simulation program has high reliability and the obtained data has high reference value. At present, it is very difficult and costly to perform dynamic cloud dispersion tests. However, this model can predict the cloud radius, velocity, concentration, and particle size at different falling speeds, providing a research basis and reference for the actual experiment and application.

4 Conclusion

The present study proposed a model for predicting the fuel cloud dispersion that is more efficient than traditional models. It comprises six parts: breaking of the center tube shell structure, breaking of the liquid fuel ring, fuel secondary crushing process, droplet movement, center tube detonation product expansion model, and axial expansion effect correction model.

The model was validated by experimental data for static and dynamic dispersion. The predictions based on the model were superior to traditional models because some important parameters can be calculated in a few minutes such as the cloud radius, velocity, and particle size dispersion at different falling speeds, which described the dispersal process well. This study provides fuel cloud dispersion with an efficient prediction tool that can be helpful in the risk management of fire and denotation on the project, guiding practical engineering research.

Moreover, an umbrella-like cloud was obtained by applying a fall speed of 0.12 Mach number; a center hollow area in the cloud was obtained, which was closer to the actual morphology of the fuel cloud. The results show that the model contributes to the study of the dynamic cloud detonation in which few studies currently exist.

References

[1] D. R. Gardner, *Near-Field Dispersion Modeling for Liquid Fuel-Air-Explosive*, Sandia National Laboratories Report No. SAND 90-0686, **1990**.

[2] M. W. Glass, *Far-Field Dispersion Modeling for Fuel-Air-Explosive Devices*, Sandia National Laboratories Report. No. SAND90–528, **1990**.

[3] D. L. Frost, J. F. Ruel, Z. Zarei, S. Goroshin, Y. Gregoire, F. Zhang, A. Milne, A. Longbottom, Explosive Formation of Coherent Particle Jets, *J. Phys. Conf. Ser.* **2014**, *500*, 112026.

[4] R. C. Ripley, F. Zhang, Jetting Instability Mechanisms of Particles from Explosive Dispersal, *J. Phys. Conf. Ser.* **2014**, *500*, 152012.

[5] F. D. Alonso, E. G. Ferradás, J. F. S. Pérez, A. M. Aznar, J. R. Gimeno, J. M. Alonso, Characteristic Overpressure-Impulse-Distance Curves for Vapor Cloud Explosions Using the TNO Multi-Energy Model, *J. Hazard. Mater.* **2006**, *A137*, 734–741.

[6] D. L. Frost, Y. Gregoire, S. Goroshin, F. Zhang, Jet Formation During Explosive Particle Dispersal (Meeting of the APS Division of Fluid Dynamics, Baltimore, Maryland, United States, November 20–22, 2011), *American Physical Society.* **2011**, *56*, 18.

[7] K. Xue, F. Li, C. Bai, Explosively Driven Fragmentation of Granular Materials, *Eur. Phys. J.* **2013**, *E. 36*, 95.

[8] A. M. Milne, E. Floyd, A. W. Longbottom, P. Taylor, Dynamic Fragmentation of Powders in Spherical Geometry, *Shock Waves.* **2014**, *24*, 501–513.

[9] S. Goroshin, D. L. Frost, R. C. Ripley, F. Zhang, Measurement of Particle Density During Explosive Particle Dispersal, *Propellants Explos. Pyrotech.* **2016**, *41*, 245–253.

[10] J. Loiseau, Q. Pontalier, A. M. Milne, S. Goroshin, D. L. Frost, Terminal Velocity of Liquids and Granular Materials Dispersed by a High Explosive, *Shock Waves*, **2018**, *28*, 473–487.

[11] H. Grisaro, A. N. Dancygier, Numerical Study of Velocity Distribution of Fragments Caused by Explosion of a Cylindrical Cased Charge, *Int. J. Impact Eng.* **2015**, *86*, 1–12.

[12] H. Wang, X. Sun, G. Rao, G. Jian, L. Xie, The Critical Energy of Direct Initiation in Liquid Fuel-Air and Liquid Fuel-RDX Powder-Air Mixtures in a Vertical Detonation Tube, *Propellants Explos. Pyrotech.* **2014**, *39*, 597–602.

[13] Q. Zhang, C. Bai, Q. Liu, Z. Wang, Near Area Dispersion of Fuel Air Explosive Under the Action Of Uncoupled Charge Explosion, *Ballistics Journal* **2000**, *12*, 26–29.

[14] Z. Wang, H. Chen, Y. Liu, Y. Guo, Numerical Simulation of the Inert Particles Driven by Explosives, *Acta Armamentarii* **2010**, *S1*, 112–117.

[15] C. H. Bai, Y. Wang, J. P. Li, M. Chen, Influences of the Cloud Shape of Fuel-Air Mixtures on the Overpressure Field, *Shock & Vibration* **2016**, 1–7.

[16] G. I. Taylor, G. K. Batchelor, Scientific Papers, Iii: Aerodynamics and the Mechanics of Projectiles and Explosions, Cambridge University Press, **1963**.

[17] A. M. Milne, C. Parrish, I. Worland, Dynamic Fragmentation of Blast Mitigants, *Shock Waves* **2010**, *20*, 41–51.

[18] O. G. Engel, Fracmentation of Water Drops in the Zone Behind an Air Shock, *J. Res. Natl. Bur. Stand.* **1958**, *60*, 245.

[19] S. Eidelman, A. Burcat, Evolution of a Detonation Wave in a Cloud of Fuel Droplets, I – Influence of Igniting Explosion, *AIAA J.* **1980**, *18*, 1103–1109.

[20] J. O. Hinze, Fundamentals of the Hydrodynamic Mechanism of Splitting in Dispersion Processes, *AIChE J.* **1955**, *1*, 289–295.

[21] S. Corrsin, J. L. Lumley, On The Equation of Motion for a Particle in a Turbulent Fluid, *Appl. Sci. Res.* **1956**, *6*, 114–116.

[22] M. R. Maxey, J. J. Riley, Equation of Motion for a Small Rigid Sphere in a Nonuniform Flow, *Phys. Fluids* **1983**, *26*, 883–889.

[23] K. F. Cen, J. R. Fan, The Analyis of the Forces Acting on Coal Particles and the Trajectories in the Gas Flows. , *J. Zhejiang University (Natural Science)* **1987**, *6*, 6–16.

[24] A. B. Basset, Treatise On Hydrodynamics, Deighton Bell, London, **1888**, *2*, 285–297.

[25] P. G. Saffman, The Lift on a Small Sphere in a Slow Shear, *J. Fluid Mech.* **1965**, *22*, 385–400.

[26] S. Elghobashi, G. C. Truesdell, Direct Simulation of Particle Dispersion in a Decaying Isotropic Turbulence, *J. Fluid Mech.* **1992**, *242*, 655.

[27] A. A. Borisov, B. E. Gel Fand, S. A. Gubin, S. M. Kogarko, A. L. Podgrebenkov, Detonation Reaction Zone in Two-Phase Mixtures, *Combust. Explos.. Shock Waves* **1970**, *6*, 327–336.

[28] R. Clift, J. R. Grace, M. E. Weber, Bubbles, Drops and Particles, Academic Press, New York, **1978**.

[29] L. Schiller, A. Naumann, A Drag Coefficient Correlation, *Zeitschrift des Vereins Deutscher Ingenieure* **1935**, *77*, 318–320.

[30] C. Y. Wen, Y. H. Yu, Mechanics of Fluidization, *Chemical Engineering Progress Symposium Series* **1966**, *62*, 100.

[31] S. Z. Zhang, Dynamics of Explosion and Impact, *Ordnance Industry Press* Beiing, China, **1993**, *140*.

[32] F. Zhang, R. C. Ripley, A. Yoshinaka, C. R. Findlay, J. Anderson, B. von Rosen, Large-Scale Spray Detonation and Related Particle Jetting Instability Phenomenon [J]. *Shock Waves* **2015**, *25*, 239–254.

[33] Y. Wang, C. Bai, J. P. Li, Dynamic Cloud Formation and the Characteristics of Detonation Field, *Chinese J. Energ. Mater.* **2017**, *25*, 466–471.

[34] http://www.globalsecurity.org/military/systems/munitions/fae.htm.